

1 **Centennial to millennial-scale monsoon changes since the last deglaciation linked to**
2 **solar activities and North Atlantic cooling**

3 **Xingxing Liu^{1,2*}, Youbin Sun^{1,2,3*}, Jef Vandenberghe⁴, Peng Cheng^{1,3,5}, Xu Zhang^{6,7}, Evan J**
4 **Gowan⁷, Gerrit Lohmann⁷, Zhisheng An^{1,2,3}**

5 ¹State Key Laboratory of Loess and Quaternary Geology, Institute of Earth Environment,
6 Chinese Academy of Sciences, Xi'an, 710061, China

7 ²CAS Center for Excellence in Quaternary Science and Global Change, Chinese Academy of
8 Sciences, Xi'an, 710061, China.

9 ³Institute of Global Environmental Change, Xi'an Jiaotong University, Xi'an, 710049, China

10 ⁴Institute of Earth Sciences, Vrije Universiteit, De Boelelaan 1085, 1081 HV Amsterdam, The
11 Netherlands

12 ⁵Xi'an AMS Center of IEECAS, And Shaanxi Provincial Key Laboratory of Accelerator Mass
13 Spectrometry and Application, Xi'an, 710061, China

14 ⁶Key Laboratory of Western China's Environmental Systems (Ministry of Education), College of
15 Earth and Environmental Sciences, Lanzhou University, Lanzhou, 730000, China

16 ⁷Alfred Wegener Institute Helmholtz Centre for Polar and Marine Research, Bussestrasse 24, D-
17 27570 Bremerhaven, Germany

18 *Corresponding author: Xingxing Liu (liuwx@ieecas.cn) and Youbin Sun (sunyb@ieecas.cn)

19 **Abstract**

20 Rapid monsoon changes since the last deglaciation remain poorly constrained due to the scarcity
21 of geological archives. Here we present a high-resolution scanning X-ray fluorescence (XRF)
22 analysis of a 13.5-m terrace succession on the western Chinese Loess Plateau (CLP) to infer
23 rapid monsoon changes since the last deglaciation. Our results indicate that Rb/Sr and Zr/Rb are
24 sensitive indicators of chemical weathering and wind sorting, respectively, which are further
25 linked to the strength of the East Asia summer monsoon (EASM) and the East Asia winter
26 monsoon (EAWM). During the last deglaciation, two cold intervals of the Heinrich event 1 and
27 Younger Dryas were characterized by intensified winter monsoon and weakened summer
28 monsoon. The EAWM gradually weakened since the beginning of the Holocene, while the
29 EASM remained steady till 9.9 ka and then grew stronger. Both the EASM and EAWM intensity
30 were relatively weak during the middle Holocene, indicate a mid-Holocene climatic optimum.
31 Rb/Sr and Zr/Rb exhibit an anti-phase relationship between the summer and winter monsoon
32 changes on centennial timescale during 16~1 ka BP. Comparison of these monsoon changes with
33 solar activity and North Atlantic cooling events reveals that both factors can lead to abrupt
34 changes on the centennial timescale in the early Holocene. During the late Holocene, North
35 Atlantic cooling became the major forcing of centennial monsoon events.

36 **Keywords:** Chinese Loess Plateau; East Asian summer monsoon; East Asian winter monsoon;
37 Elemental ratios; Centennial to millennial variability; Solar activities; North Atlantic cooling

38 **1 Introduction**

39 The East Asian monsoon (EAM) is one of the most important atmospheric circulation
40 systems linked to climate changes over high- and low-latitude regions of the Northern

41 Hemisphere (Ding, 1994). It consists of summer and winter monsoons (EASM and EAWM) with
42 significantly seasonal changes in moisture transportation and wind direction. During the past
43 three decades, variability of the rain-bearing EASM on millennial to centennial time scales has
44 been investigated extensively from cave deposits (Dykoski et al., 2005; Wang et al., 2005; Cheng
45 et al., 2016), loess sequences (An et al., 1991; Ding et al., 1995; Sun et al., 2006, 2016; Kang et
46 al., 2018), lake sediments (Yancheva et al., 2007; An et al., 2012; Chen et al., 2015; Liu et al.,
47 2016), marine sediments (Huang et al., 2011), and model simulations (Wen et al., 2016). These
48 previous studies show a series of oscillations and/or abrupt events, such as the 4.2, 8.2, 9.2 and
49 10.3 ka events. These records suggest the summer monsoon variations are not only induced by
50 changes in Northern Hemisphere summer insolation, but also strongly modulated by internal
51 land-ocean-air interactions of the Earth-climate systems (e.g., An et al., 2015).

52 Unlike abundant proxies of the EASM variability, high-resolution records reflecting
53 millennial to centennial EAWM variability are still sparse. Though various proxies from
54 different paleoclimatic archives have been used to document EAWM evolution since the last
55 deglaciation, great differences were observed on the inferred winter monsoon changes and
56 forcing mechanisms (Yancheva et al., 2007; Huang et al., 2011; Wang et al., 2012; Li and
57 Morrill, 2015; Kang et al., 2018) . There are four primary factors contribute to these conflicting
58 records. First, the loess-paleosol record on the Chinese Loess Plateau (CLP) (Sun et al., 2012;
59 Kang et al., 2018) or marine sediments from the South China Sea (Huang et al., 2011) are not of
60 sufficiently high resolution to detect centennial to millennial EAWM changes due to relatively-
61 low sedimentation rates. Second, the sensitivity of various archives and proxies to changes in the
62 monsoon intensity is different (e.g., Yancheva et al., 2007; Huang et al., 2011; Kang et al., 2018).
63 Some environmental proxies commonly show different amplitudes and timing of variation, likely

64 reflecting the fact that they respond to different aspects of climate and environment (temperature,
65 wind and precipitation). Third, the proxies used for the EAWM remains controversial, such as
66 whether Titanium (Ti) in Huguang Maar Lake is a proxy for local hydrology or EAWM intensity
67 (Yancheva et al., 2007; Zhang et al., 2007). Fourth, uncertain chronologies from diverse natural
68 archives (e.g., loess, lake, and marine) may lead to timing mismatch on centennial timescales.

69 Wen et al. (2016) performed a set of long-term transient simulations that suggest the EASM
70 and EAWM are anti-correlated on millennial timescales in response to North Atlantic meltwater
71 forcing during the last 21 ka. However, there is still a lack of high-resolution proxies to support
72 this modelling result. This hampers our understanding of the effects of external solar forcing and
73 internal meltwater feedbacks (Li and Morrill, 2015; Wen et al., 2016). Though numerous studies
74 have focused on the rapid climate changes on the EASM and EAWM since the last deglaciation,
75 significant differences and asynchronous changes still exist (e.g., Wang et al., 2005; Yancheva et
76 al., 2007; Huang et al., 2011; An et al., 2012; Chen et al., 2015). Therefore, it is crucial to
77 investigate high-resolution, independent proxies with robust chronology of the summer and
78 winter monsoon intensities in one single archive to improve our understanding of rapid monsoon
79 changes and dynamics in particular the centennial to millennial variability and coherent forcing
80 mechanisms.

81 In this study, we investigate a thick terrace succession on the western CLP to determine
82 EAWM and EASM variability since the last deglaciation for the first time. Our results provide
83 valuable insights into the relationship between the EAWM and EASM variability at centennial to
84 millennial timescales using high-resolution (5-mm interval) elemental records obtained by X-ray
85 fluorescence (XRF) core scanning. We compare the elemental ratios (Zr/Rb and Rb/Sr) with

86 other paleo-records of abrupt monsoon changes to determine the links with external solar forcing
87 and internal feedbacks.

88 **2 Materials and Methods**

89 The Dadiwan section (DDW, 35.02°N, 105.8°E, 1454 m a.s.l) in Qin'an County, Gansu
90 Province is located on the first terrace of the Wei River on the western CLP (Fig. 1A). Fluvio-
91 aeolian sediments are thick and widely deposited on river terraces of the Wei River and its
92 tributaries in this area (Fig. 1B). From 1981 to 2010, the mean annual precipitation and mean
93 annual temperature in Qin'an County is 507.3 mm and 10.4°C, respectively (Meteorological data
94 come from the national daily dataset of surface weather profile provided by the National
95 Meteorological Data Center, <http://data.cma.cn/data/>). Dadiwan is known as the oldest example
96 and type site of the “Dadiwan cultural” or “Laoguantai cultural” complex, which is the
97 westernmost expression of early millet agriculture in North China. Previous studies in Dadiwan
98 area based on organic carbon and pollen revealed that the middle Holocene was the most humid
99 interval since the last deglaciation (Feng et al., 2004). During April 2015, we retrieved a 13.5-m
100 core using a hydraulic-static drilling rig with a dual-tube (outer and inner tubes) core barrel. The
101 core recovery rate was almost 100%, though some cores were slightly compressed (Fig. 1C).

102 After splitting the cores into a working and archive half with a Geotek core splitter, the
103 surface of the cores was carefully smoothed to reduce scanning errors caused by irregularities
104 from core slicing (Fig. 1C). The split core surface was subsequently covered with a 4 µm
105 Ultralene film during core logging in order to avoid contamination of the XRF detector window
106 and to prevent desiccation of the core surface. The split cores were scanned every 5-mm using an
107 Avaatech XRF core scanner at the Institute of Earth Environment, Chinese Academy of Sciences.

108 The elements measured range from Al to Fe in the periodic table were detected at an X-ray
109 voltage of 10 kV, Co to Mo at 30 kV, and Te to Ba at 50 kV (Richter et al., 2006; Weltje and
110 Tjallingii, 2008). On the basis of the processed model, we used the WinAxil and WinAxilBatch
111 software to calculate the element counts (counts per second, CPS) as peak integrals and applied
112 background subtraction. The quality of every single spectrum and peak integral can be easily
113 checked with the χ^2 value (Van Espen et al., 1977). As the variation in element concentrations of
114 loess can be related to grain size sorting and chemical weathering (Chen et al., 1999, 2006; Peng
115 and Guo, 2001), three elements (Rb, Zr and Sr) with high concentrations and low analytical
116 uncertainties which were detected at 30 kV are discussed in this study.

117 After core scanning, sub-samples were taken at contiguous 1-cm intervals. A total of 1350
118 sub-samples were obtained for grain size and magnetic susceptibility analyses (see Fig. 2 in Liu
119 et al., 2018 for a detailed description). A rough chronology of the DDW section was established
120 by accelerator mass spectrometer (AMS) ^{14}C dates based on five total organic carbon from bulk
121 sediments (Liu et al., 2018). In this study, seven additional ^{14}C dates from bulk organic matter
122 were obtained in order to get more reliable age control. The samples were pretreated with 1M
123 HCl (2 hr, 60°C) to remove carbonate, and then were thoroughly rinsed with distilled water
124 (Zhou et al., 2006). Pretreated samples and CuO powder were placed into 9-mm quartz tubes,
125 evacuated to 1×10^{-5} Torr, and then combusted. The pure CO_2 was collected using liquid nitrogen
126 and reduced to graphite for AMS dating. For the AMS analysis, the CO_2 was reduced to graphite
127 using Zn/Fe catalytic reduction. All these selected 12 samples were analyzed using a 3MV
128 tandem accelerator at the Xi'an accelerated mass spectroscopy center and calibrated using calib.
129 7.0.2 (Reimer et al., 2004).

130 3 Results

131 Based on soil structure, color, magnetic susceptibility and grain size, the 13.5-m DDW core
132 can be divided lithologically into three sub-units from bottom to top: 13~13.5 m, fluvial
133 sediments; 6~13 m, loess deposits; 0~6 m, paleosol interbedded with four weakly weathered
134 paleosol layers (Fig. 2A). The 12 radiocarbon ages have a linear correlation with depth. This is
135 consistent with a continuous sediment accumulation under a stable environment between 16~1
136 ka BP. The age-depth model is constructed using linear regression ($y=1.1465x+1.2546$,
137 $R^2=0.9921$), x is the depth in m, y is the calculated age (cal ka BP) (Fig. 2B). Since the dating
138 errors ranges from 24 to 53 years and our 1-cm sampling strategy yields a time resolution of
139 about 12 year, it is reasonable to discuss centennial to millennial scale monsoon variations since
140 the last deglaciation based on our high-resolution results.

141 The magnetic susceptibility displays a stepwise increase from $\sim 13.7 \times 10^{-8} \text{m}^3 \text{kg}^{-1}$ below 6 m
142 to $15.5 \sim 138.6 \times 10^{-8} \text{m}^3 \text{kg}^{-1}$ above 6 m, with maximum values at three strongly weathered soil
143 layers (Fig. 2C). Mean grain size, however, exhibits a two-stage variability except for the lower
144 0.5-m fluvial sandy layers (not shown here because it goes off the scale) (Fig. 2D); The lower
145 part (13.5~6 m) exhibits large fluctuations ($7.9 \sim 121.3 \mu\text{m}$) while the loess-paleosol alternations
146 (6~0 m) show small fluctuations ($6.4 \sim 28.8 \mu\text{m}$). Generally, high magnetic susceptibility
147 corresponds to fine mean grain-size, but the abrupt MS increase around 6 m is different from the
148 gradual fining of the mean grain size between 8.2~6.8 m.

149 Similar to variations of magnetic susceptibility and grain-size, Rb, Sr and Zr exhibit
150 significant variability, with ranges of 3400~8827 cps for Rb (Fig. 2E), 7000~40000 cps for Sr
151 (Fig. 2F), and 7000~30000 cps for Zr (Fig. 2G). Low Rb/Sr ratio values correspond to low
152 magnetic susceptibility, with values in the range from 0.18 to 0.6, revealing distinct pedogenic

153 weathering effects. (Fig. 2H). The variation of the Zr/Rb ratio ranges from 1.2 to 5.8. High Zr/Rb
154 ratios occur where grain-size is coarse, suggesting grain-size sorting effects (Fig. 2I).

155 **4 Discussion**

156 4.1 EAM variability on orbital timescale since the last deglaciation

157 A number of elements (e.g. Al, Si, K, Ca, Ti, Fe, Mn, Rb, Zr, Sr) based on scanning XRF
158 have been used to acquire information of past climatic and environmental changes (Richter et al.,
159 2006; Liang et al., 2012; Sun et al., 2016). However, the interpretation of lighter elements data
160 require careful consideration due to the instrument detection limits and analytical uncertainties
161 (e.g. organic matter and water content) (Richter et al., 2006). Considering the sedimentary
162 characteristics and geochemical behavior of Zr (commonly abundant in coarse-grained sediments
163 and resistant to weathering), Rb (enriched in clay deposits, relatively stable) and Sr (easily
164 mobilized during chemical weathering), the ratios of Zr/Rb can be an indicator of grain-size
165 sorting and Rb/Sr is an indicator of chemical weathering (Chen et al., 1999, 2006; Peng and Guo,
166 2001). Previous studies demonstrated that grain size and magnetic susceptibility of loess-
167 paleosol sequences have been widely used as proxies for winter and summer monsoon,
168 respectively (An et al., 1991; Ding et al., 1995; Sun et al., 2006). Taking into account the ratios of
169 Zr/Rb and Rb/Sr are highly consistent with grain-size and magnetic susceptibility (Fig. 2), we
170 used Zr/Rb and Rb/Sr ratios as proxies for EAWM and EASM intensity, respectively.

171 The Zr/Rb and Rb/Sr ratios reveal significant millennium- to centennial-scale variability
172 (Fig. 3). During the last deglaciation, the Zr/Rb ratio has large-amplitude, high-frequency
173 fluctuations, in contrast to small-amplitude and low-frequency oscillations during the Holocene
174 (Fig. 3B). The Rb/Sr ratio exhibits relatively small-amplitude fluctuations during the last

175 deglaciation to early Holocene (16~10 ka BP) and mid-to-late Holocene (7-1 ka BP). In the early
176 to mid-Holocene (10-7 ka BP), there are large amplitude fluctuations (Fig. 3C). During the last
177 deglaciation, two cold intervals of the Heinrich event 1 (16~14.8 ka) and Younger Dryas (YD,
178 12.8~11.7 ka) were characterized by intensified EAWM (Fig. 3B) and weakened EASM (Fig.
179 3C). The period from 14.8~12.8 ka with strong EASM/weak EAWM, which might be temporally
180 consistent with the Bølling-Allerød (BA) warming episode. A rapid weakening of the EAWM
181 occurred during the early Holocene, and then reached a minimum during 9.9~4.8 ka in the
182 middle Holocene (Fig. 3B). Minimum EASM intensity occurs from 11.7~9.9 ka during the early
183 Holocene, and increased to the highest level during during 8~4.8 ka during the middle Holocene
184 (Fig. 3C). In the late Holocene, a shift of the monsoon intensity is evident in both Zr/Br and
185 Rb/Sr, EASM continue to moderate while EAWM increased gradually.

186 On orbital time scales, changes in the EAWM have been linked to changes in ice volume in
187 the Northern Hemisphere (Ding et al., 1995; Liu and Ding, 1998; Porter, 2001). It has been
188 shown that Northern Hemisphere ice sheets in land were larger during the early-middle Holocene
189 than during the late Holocene (Dyke and Prest, 1987; Kutzbach et al., 1998). The winter
190 insolation in Northern Hemisphere is lower during early Holocene than during late Holocene
191 (Berger and Loutre, 1991). Such change in the size of ice sheets and the insolation should have
192 caused a strengthening of the EAWM during the early Holocene. However, the intensity of
193 EAWM appears to be different between the DDW and the Lake Huguang Maar (Fig. 3A)
194 (Yancheva et al., 2007) in southern China during the early Holocene. This discrepancy might
195 attribute to the ice sheets at high latitudes did not influence the EAWM over southern China as
196 strongly as they influenced EAWM expression in northern China during the early Holocene.

197 Orbital trend of EASM intensity from DDW generally resembles the Pollen-based annual
198 precipitation (PANN) reconstructed from Gonghai Lake (Fig.3D) (Chen et al., 2015; Liu et al.,
199 2015, 2017), indicate a mid-Holocene climatic optimum (Liu et al., 2015). This suggests that
200 EASM intensity not only follows changes in insolation inferred from the Lake Qinghai summer
201 monsoon index (SMI) (Fig. 3E) (An et al., 2012) and stalagmite $\delta^{18}\text{O}$ records in eastern China
202 (Fig. 3F) (Dykoski et al., 2005; Wang et al., 2005), but was also strongly moderated by the
203 internal feedback processes such as continuous freshwater input into the North Atlantic caused
204 by the remnant melting Laurentide ice sheet (Chen et al., 2015). In addition to this, asynchronous
205 changes among these proxies can be possible due to varied sensitivity of these proxies and
206 archives to changes in the monsoon intensity (Caley et al., 2014).

207 4.2 Centennial monsoon variability since the last deglaciation

208 EAWM and EASM intensity are anti-phase at both millennial- and centennial-scale since
209 the last deglaciation (Fig. 3). That is, when the EAWM is strong, the EASM is weak. A series of
210 strong EAWM and weak EASM events (e.g., H1, YD, 11.1, 10.1, 9.3, 8.2, 7.3, 6.7, 5.9, 4.6 and
211 2.1 ka) can be identified from Zr/ Rb and Rb/Sr values. The mechanism of this anti-phase
212 relationship between EAWM and EASM on millennial to centennial scale can potentially be
213 ascribed to the release of meltwater into the North Atlantic and the resulted change in the
214 Atlantic Meridional Overturning Circulation (AMOC) (Broecker et al., 1992; Alley et al., 1997;
215 Bond et al., 2001; Wen et al., 2016). In addition, previous studies also suggest that the change in
216 the solar activity partly influences EAWM/EASM strength in centennial timescale, through the
217 the migration of annual mean position of the intertropical convergence zone (ITCZ) during
218 summer times (Haug et al., 2001; Dykoski et al., 2005; Wang et al., 2005; Yancheva et al., 2007;
219 Steinhilber et al., 2012), and changes in the meridional temperature gradient during winter times

220 (Xiao et al., 2006; Liu et al., 2009; Sagawa et al., 2014). However, some of the intervals (e.g.,
221 YD, 11.1, 6.7 ka) are more distinct in the Zr/Rb ratio, while some intervals such as the 7.3 ka
222 event is more distinct in the Rb/Sr ratio. The differences between the two proxies records during
223 these abrupt intervals shows that they have variable sensitivity to monsoonal wind and
224 precipitation intensity changes (Sun et al., 2012; Chen et al., 2015).

225 The centennial-scale winter monsoon changes since the last deglaciation reconstructed at
226 DDW are partially consistent with previous high-resolution Ti records from Lake Huguang Maar
227 in southern China (Fig. 3A) (Yancheva et al., 2007). This support that the record of Ti counts can
228 be a measure of winter monsoon strength although it is still controversial due to the provenance
229 of the lake sediments (Yancheva et al., 2007; Zhang et al., 2007). Some of the strong winter
230 monsoon intervals (e.g., 7.3 ka) are not significant in the Lake Huguang Maar, which indicate
231 that DDW, located in northern China, is more sensitive to the EAWM system. Another
232 possibility for this discrepancy is that control points between 8 ka and 4ka are lacking in the
233 Lake Huguang Maar (Fig. 3A).

234 Compared with other summer monsoon proxy records in China, the centennial-scale EASM
235 changes at DDW are consistent with the PANN reconstructed from Gonghai Lake (Fig.3D)
236 (Chen et al., 2015; Liu et al., 2015, 2017) and SMI from Lake Qinghai (Fig. 3E) (An et al., 2012).
237 Almost all the weak summer monsoon intervals, within dating errors, appear to coincide with
238 major changes in the PANN reconstruction and SMI. It is worth noting that 8.2 ka event was not
239 significant in the Gonghai (Fig. 3D) and Qinghai Lake (Fig. 3E). This could be ascribed to age
240 model discrepancies, or the variable sensitivity of different proxies to changes in monsoon
241 intensity (Chen et al., 2015). However, there are some discrepancies between Rb/Sr ratio of
242 DDW and the $\delta^{18}\text{O}$ record from Dongge Cave stalagmites in eastern China (Fig. 3F)

243 (Dykoski et al., 2005; Wang et al., 2005). This discrepancy might attribute to the controversial
244 paleoclimatic significance of $\delta^{18}\text{O}$ records from caves in southern China, or the North-South
245 differences for the monsoon intensity (Caley et al., 2014; Tan, 2014; Liu et al., 2015; Chen et al.,
246 2016). Therefore, the weak EASM intervals existing in all these three different regions (CLP,
247 northeast of Tibetan Plateau and eastern China) may have recorded centennial EASM variability
248 since the last deglaciation.

249 4.3 Links between solar forcing and high-latitude climate changes

250 We removed the long-term trend of Zr/Rb and Rb/Sr ratios to investigate the high frequency
251 components of the signal (<1 kyr), then compare the results with the North Atlantic hematite-
252 stained grains records (HSG) (Bond et al., 2001) and atmospheric ^{14}C production rate ($\Delta^{14}\text{C}$)
253 (Reimer et al., 2013) (Fig. 4a). HSG is a tracer of drift ice in the North Atlantic, high values of
254 HSG indicate cold conditions (Bond et al., 2001). Higher values of atmospheric $\Delta^{14}\text{C}$ represent
255 weak solar activity and vice versa (Stuiver and Quay, 1980). High-frequency components of the
256 EAWM (Fig. 4B) and EASM (Fig. 4C) proxies from DDW exhibit large-amplitude fluctuations
257 during the early Holocene (11.5~7 ka), while the amplitude variations were more moderate
258 during the late Holocene (7~1 ka), especially the Rb/Sr ratio. All the strong winter and weak
259 summer monsoon intervals from DDW records can either be correlated with HSG (Fig. 4A), or
260 with high atmospheric $\Delta^{14}\text{C}$ (Fig. 4D). This indicate possible relationship with Northern
261 Hemisphere cooling and solar activity.

262 During the early Holocene (11.5~7 ka), all of the strong EAWM/weak EASM intervals (e.g.,
263 11.1, 10.1, 9.3, 8.2, 7.3 ka BP) within the limits of dating error are correlated with HSG (Fig. 4A)
264 and high $\Delta^{14}\text{C}$ (Fig. 4D). High similarity of these records suggests that the North Atlantic

265 cooling events and solar activity probably simultaneously affect the EAM systems on centennial
266 timescales. During the late Holocene (7~1 ka), all the strong EAWM (Fig. 4B) and weak EASM
267 (Fig. 4C) events (e.g., 6.7, 5.9, 4.6, 3.3, 2.8 and 2.1 ka BP) correspond well to the abrupt events
268 in the North Atlantic region. This indicates that North Atlantic cooling plays an important role in
269 driving the centennial monsoon changes during the late Holocene. The 3.3 and 2.8 ka events are
270 also correlated well with high $\Delta^{14}\text{C}$, which indicate solar forcing also plays a role during those
271 times.

272 In order to further confirm the possible link of monsoon variability with internal North
273 Atlantic feedbacks and external solar forcing on centennial-scale, spectral analyses were
274 conducted on these proxies for the early (11.5~7 ka) (Fig. 4b) and late (7~1 ka) (Fig. 4c)
275 Holocene (Fig. 4). The spectral results reveal that the Zr/Rb and Rb/Sr records both display a
276 prominent periodicity at 1.0 kyr (Fig. 4F and G). This matches with the cycle of HSG (Fig. 4E)
277 and $\Delta^{14}\text{C}$ (Fig. 4H) during the early Holocene. The similarity in periodicity further confirm the
278 link of centennial EAM variability to North Atlantic cooling and solar activities during the early
279 Holocene (11.5~7 ka). However, the dominant periodicity (~1.27 kyr) of HSG, Zr/Rb and Rb/Sr
280 records are not evident in the $\Delta^{14}\text{C}$ spectrum during the late Holocene (7~1 ka) (Fig.4I-L),
281 implying that solar forcing is not the dominant cause of centennial monsoon variability during
282 this period.

283 North Atlantic cooling and solar activity are two commonly accepted drivers of centennial
284 climate variability. There is a teleconnection between rapid monsoon changes and abrupt events
285 in the North Atlantic region (the ocean thermohaline circulation) (Broecker et al., 1992; Alley et
286 al., 1997; Bond et al., 2001; Wang et al., 2005). The strength of the Siberian High, located north
287 of our DDW section, increases when the North Atlantic is in a cold mode (Gong et al., 2001).

288 The ITCZ shifted southward due to changes in the AMOC and temperature gradients across the
289 northern hemisphere. When ITCZ shifted southward, the EASM weakened and EAWM
290 strengthened (Broccoli et al., 2006; Sun et al., 2012; Wen et al., 2016). Speleothem records from
291 China (Dykoski et al., 2005; Cheng et al., 2006; Wang et al., 2008) and many model simulations
292 (Chiang and Bitz 2005; Broccoli et al. 2006) support this.

293 The change in solar activity could contribute to the regional monsoon variability by
294 affecting low-latitude hydrological processes (Liu et al. 2009; Yan et al. 2015). Specifically,
295 decreased summer insolation results in changes to the land-ocean thermal contrast. The sea
296 surface temperature in the western tropical Pacific decreases and the Northwest Pacific
297 Subtropical High weakens (Liu et al., 2003; Cai et al., 2010). This decreased thermal contrast
298 would result in a southward migration of the ITCZ and also weaken the EASM strength by
299 reducing the monsoon moisture transport from the tropical ocean to the continent in low latitudes
300 (Liu et al. 2009; Yan et al. 2015). Since changes in solar output are large at centennial-scale
301 during the early Holocene, this may amplify the solar output effect due to nonlinear responses
302 and feedback processes of the climate system (Mohtadi et al., 2016). During the late Holocene
303 (7~1 ka), there is a decrease of summer insolation and the small-amplitude fluctuations of solar
304 activities (Fig. 4D) (Berger, 1978). This is probably why it play a less important role in EAM
305 system.

306 **5 Conclusions**

307 We recovered a high-resolution last deglaciation record of EAWM and EASM from terrace
308 sediments on the western CLP. Ratios of Zr/Rb and Rb/Sr are sensitive indicators of winter wind
309 intensity and chemical weathering, respectively, and thus can be regarded as an index of EAWM
310 and EASM. In general, the ratios of Rb/Sr and Zr/Rb display significant fluctuation similar to the

311 global climate characteristics since the last deglaciation (16~1 ka BP), such as Heinrich cooling
312 (H1), Bølling-Allerød warming, and Younger Dryas cooling events. Both EAWM and EASM
313 show “Holocene optimum” during the middle Holocene. A number of strong and weak monsoon
314 changes are identified by means of Zr/Rb and Rb/Sr values from DDW, such as strong
315 EAWM/weak EASM intervals around H1, YD, 11.1, 10.1, 9.3, 8.2, 5.9, 4.6, 3.3, 2.8 and 2.1 ka,
316 which reveals a negative co-variability between the EAWM and EASM on centennial timescale.
317 Our Zr/Rb and Rb/Sr records are consistent with the Ti content from Lake Huguang Maar
318 (EAWM proxy), the PANN reconstructed from Gonghai Lake and the SMI from Lake Qinghai
319 (both EASM proxies). Comparing with North Atlantic cooling and solar activity proxies, our
320 record shows that both are possible driving factors of centennial monsoon variability. North
321 Atlantic cooling events and solar activity are the dominant forcing of the EAM system during the
322 early Holocene, while North Atlantic cooling became more important during the late Holocene.

323 **Data availability**

324 All data are accessible from the authors. Correspondence and requests for materials should be
325 addressed to Xingxing Liu (liuXX@ieecas.cn).

326 **Author contributions**

327 Xingxing Liu and Youbin Sun designed the study and performed the fieldwork and experiments.
328 Jef Vandenberghe, Xu Zhang contributed to data analysis. Peng Cheng conducted the AMS ¹⁴C
329 analysis. Evan J Gowan, Gerrit Lohmann and Zhisheng An improved the manuscript with their
330 contributions.

331 **Competing interests**

332 The authors declare that they have no conflict of interest.

333 **Acknowledgments**

334 This work was supported by The National Key Research and Development Program of China
335 (2016YFA0601902), the National Science Foundation of China (41807425 and 41525008), and
336 the Open Foundation of State Key Laboratory of Loess and Quaternary Geology
337 (SKLLQG1633).

338 **References**

339 Alley, R.B., Mayewski, P.A., Sowers, T., Stuiver, M., Taylor, K.C., and Clark, P.U.: Holocene
340 climatic instability: A prominent, widespread event 8200 yr ago, *Geology*, 25 (6), 483-486,
341 1997.

342 An, Z.S., Colman, S.M., Zhou, W.J., Li, X.Q., Brown, E.T., Jull, A.J.T., Cai, Y.J., Huang, Y.S.,
343 Lu, X.F., Chang, H., Song, Y.G., Sun, Y.B., Xu, H., Liu, W.G., Jin, Z.D., Liu, X.D., Cheng,
344 P., Liu, Y., Ai, L., Li, X.Z., Liu, X.J., Yan, L.B., Shi, Z.G., Wang, X.L., Wu, F., Qiang,
345 X.K., Dong, J.B., Lu, F.Y., and Xu, X.W.: Interplay between the Westerlies and Asian
346 monsoon recorded in Lake Qinghai sediments since 32 ka, *Scientific Reports*, 2, 619, 2012.

347 An, Z.S., Kukla, G., Porter, S.C., and Xiao, J.L.: Late Quaternary dust flow on the Chinese loess
348 plateau, *Catena*, 18 (2), 125-132, 1991

349 An, Z.S., Wu, G.X., Li, J.P., Sun, Y.B., Liu, Y.M., Zhou, W.J., Cai, Y.J., Duan, A.M., Li, L.,
350 Mao, J.Y., Cheng, H., Shi, Z.G., Tan, L.C., Yan, H., Ao, H., Chang, H., and Juan, F.:
351 Global Monsoon Dynamics and Climate Change, *Annu. Rev. Annual Review of Earth and*
352 *Planetary Sciences*, 43, 29-77, 2015.

353 Berger, A.: Long term variations of daily insulations and quaternary climatic changes, *Journal of*
354 *the Atmospheric Sciences*, 35, 2362-2367, 1978.

355 Berger, A., and Loutre, M.F.: Insolation values for the climate of the last 10 million years.
356 Quaternary Science Reviews, 10(4): 297-317, 1991.

357 Berntsson, A., Rosqvist, G.C., and Velle, G.: Late-Holocene temperature and precipitation
358 changes in Vindelfjällen, mid - western Swedish Lapland, inferred from chironomid and
359 geochemical data, The Holocene, 24, 78-92. doi: 10.1177/0959683613512167, 2014.

360 Bond, G., Kromer, B., Beer, J., Muscheler, R., Evans, M.N., Showers, W., Hoffmann, S., Lotti
361 Bond, R., Hajdas, I., and Bonani, G.: Persistent solar influence on North Atlantic climate
362 during the Holocene, Science, 294 (5549), 2130-2136, 2001.

363 Broccoli, A. J., Dahl, K. A., and Stouffer, R. J.: Response of the ITCZ to Northern Hemisphere
364 cooling, Geophysical Research Letters, 33(1), 2006.

365 Broecker, W., Bond, G., Klas, M., Clark, E., and McManus, J.: Origin of the northern Atlantic's
366 Heinrich events, Climate Dynamics, 6 (3-4), 265-273, 1992.

367 Cai, Y.J., Tan, L.C., Cheng, H., An, Z.S., Edwards, R.L., Kelly, M.J., Kong, X.G., and Wang,
368 X.F.: The variation of summer monsoon precipitation in Central China since the last
369 deglaciation, Earth and Planetary Science Letters, 291 (1), 21-31, 2010.

370 Caley, T., Roche, D.M., and Renssen, H.: Orbital Asian summer monsoon dynamics revealed
371 using an isotope-enabled global climate model. Nature communications, 5: 5371, 2014.

372 Chen, F., Xu, Q., Chen, J., Birks, H.J.B., Liu, J., Zhang, S., Jin, L., An, C., Telford, R.J., Cao, X.,
373 Wang, Z., Zhang, X., Selvaraj, K., Lu, H., Li, Y., Zheng, Z., Wang, H., Zhou, A., Dong, G.,
374 Zhang, J., Huang, X., Bloemendal, J., and Rao, Z.: East Asian summer monsoon
375 precipitation variability since the last deglaciation, Scientific Reports, 5, 11186, 2015.

376 Chen, J., An, Z.S., Wang, Y.J., Ji, J.F., Chen, Y., and Lu, H.Y.: Distribution of Rb and Sr in the
377 Luochuan loess-paleosol sequence of China during the last 800 ka implications for
378 paleomonsoon variations, *Science China Earth Sciences*, 42, 225-232, 1999.

379 Chen, J., Chen, Y., Liu, L., Ji, J., Balsam, W., Sun, Y., and Lu, H.: Zr/Rb ratio in the Chinese
380 loess sequences and its implication for changes in the East Asian winter monsoon strength,
381 *Geochimica et Cosmochimica Acta*, 70, 1471-1482, 2006.

382 Chen, J.H., Rao, Z.G., Liu, J.B., Huang, W., Feng, S., Dong, G.H., Hu, Y., Xu, Q.H., Chen, F.H.:
383 On the timing of the East Asian summer monsoon maximum during the Holocene—Does
384 the speleothem oxygen isotope record reflect monsoon rainfall variability?. *Science China
385 Earth Sciences*, 59(12): 2328-2338, 2016.

386 Cheng, H., Edwards, R. L., Wang, Y., Kong, X., Ming, Y., Kelly, M. J., Wang, X.F., Gallup,
387 C.D., and Liu, W.G.: A penultimate glacial monsoon record from Hulu Cave and two-phase
388 glacial terminations, *Geology*, 34(3), 217-220, 2006.

389 Cheng, H., Edwards, R.L., Sinha, A., Spotl, C., Yi, L., Chen, S.T., Kelly, M., Kathayat, G.,
390 Wang, X.F., Li, X.L., Kong, X.G., Wang, Y.J., Ning, Y.F., and Zhang, H.W.: The Asian
391 monsoon over the past 640,000 years and ice age terminations, *Nature*, 534, 640-646, 2016.

392 Chiang, J.C.H., and Bitz, C.M.: Influence of high latitude ice cover on the marine Intertropical
393 Convergence Zone, *Climate Dynamics*, 25, 477-496, 2005.

394 Ding, Y.H.: *Monsoon over China*, Kluwer Academic, p. 420, 1994.

395 Ding, Z.L., Liu, T.S., Rutter, N.W., Yu, Z.W., Guo, Z.T., and Zhu, R.X.: Ice-volume forcing of
396 East Asian winter monsoon variations in the past 800,000 years, *Quaternary Research*, 44
397 (2), 149-159, 1995.

398 Dyke, A., and Prest, V.: Late Wisconsinan and Holocene history of the Laurentide ice sheet[J].
399 *Géographie physique et Quaternaire*, 41(2): 237-263, 1987.

400 Dykoski, C.A., Edwards, R.L., Cheng, H., Yuan, D.X., Cai, Y.J., Zhang, M.L., Liu, Y.S., Qing,
401 J.M., An, Z.S., and Revenaugh, J.: A high-resolution, absolute-dated Holocene and
402 deglacial Asian monsoon record from Dongge cave, China. *Earth and Planetary Science*
403 *Letters*, 233 (1), 71-86, 2005.

404 Feng, Z.D., An, C.B., Tang, L.Y., and Jull, A.J.T.: Stratigraphic evidence of a Megahumid
405 climate between 10,000 and 4000 years BP in the western part of the Chinese Loess Plateau,
406 *Global and Planetary Change*, 43 (3), 145-155, 2004.

407 Gong, D.Y., Wang, S.W., and Zhu, J.H.: East Asian winter monsoon and Arctic Oscillation,
408 *Geophysical Research Letters*, 28 (10), 2073-2076, 2001.

409 Haug, G.H., Hughen, K.A., Sigman, D.M., Peterson, L.C., and Röhl, U.: Southward migration of
410 the intertropical convergence zone through the Holocene. *Science*, 293(5533): 1304-1308,
411 2001.

412 Huang, E., Tian, J., and Steinke, S.: Millennial-scale dynamics of the winter cold tongue in the
413 southern South China Sea over the past 26 ka and the East Asian winter monsoon,
414 *Quaternary Research*, 75 (1), 196-204, 2011.

415 Kang, S.G., Wang, X.L., Roberts, H. M., Duller, G. A., Cheng, P., Lu, Y.C., and An, Z.S.: Late
416 Holocene anti-phase change in the East Asian summer and winter monsoons, *Quaternary*
417 *Science Reviews*, 188, 28-36, 2018.

418 Kutzbach, J., Gallimore, R., Harrison, S., Behling, P., Selina, R., and Laarif, F.: Climate and
419 biome simulations for the past 21,000 years. *Quaternary Science Reviews*, 17(6-7): 473-506,
420 1998.

421 Li, Y., and Morrill, C.: A Holocene East Asian winter monsoon record at the southern edge of
422 the Gobi Desert and its comparison with a transient simulation, *Climate Dynamics*, 45,
423 1219-1234, 2015.

424 Liang, L.J., Sun, Y.B., Yao, Z.Q., Liu, Y.G., and Wu, F.: Evaluation of high-resolution elemental
425 analyses of Chinese loess deposits measured by X-ray fluorescence core scanner, *Catena*, 92:
426 75-82, 2012.

427 Liu, J., Wang, B., Ding, Q., Kuang, X., Soon, W., and Zorita, E.: Centennial variations of the
428 global monsoon precipitation in the last millennium: results from ECHO-G model, *Journal*
429 *of Climate*, 22:2356-2371, 2009.

430 Liu, J.B., Chen, J.H., Zhang, X.J., Li, Y., Rao, Z.G., and Chen, F.H.: Holocene East Asian
431 summer monsoon records in northern China and their inconsistency with Chinese stalagmite
432 $\delta^{18}\text{O}$ records. *Earth-Science Reviews*, 148: 194-208, 2015.

433 Liu, J. B., Rühland, K. M., Chen, J. H., Xu, Y. Y., Chen, S. Q., Chen, Q. M., Huang, W., Xu, Q.
434 H., Chen, F. H., and Smol, J. P.: Aerosol-weakened summer monsoons decrease lake
435 fertilization in the Chinese Loess Plateau. *Nature Climate Change*, 7, 190-194, 2017.

436 Liu, T., and Ding, Z.: Chinese loess and the paleomonsoon. *Annual review of earth and planetary*
437 *sciences*, 26(1): 111-145, 1998.

438 Liu, X.Q., Dong, H.L., Yang, X.D., Herzsuh, U., Zhang, E.L., W.Stuut, J., and Wang, Y.B.:
439 Late Holocene forcing of the Asian winter and summer monsoon as evidenced by proxy

440 records from the northern Qinghai-Tibetan Plateau. *Earth and Planetary Science Letters*,
441 280(1-4): 276-284, 2009.

442 Liu, X.X., Sun, Y.B., Vandenberghe, J., Li, Y., and An, Z.: Palaeoenvironmental implication of
443 grain-size compositions of terrace deposits on the western Chinese Loess Plateau, *Aeolian*
444 *Research*, 32, 202-209, 2018.

445 Liu, X.X., Vandenberghe, J., An, Z.S., Li, Y., Jin, Z.D., Dong, J.B., and Sun, Y.B.: Grain size of
446 Lake Qinghai sediments: implications for riverine input and Holocene monsoon variability,
447 *Palaeogeography, Palaeoclimatology, Palaeoecology*, 449, 41-51, 2016.

448 Liu, Z., Otto-Bliesner, B., Kutzbach, J., Li, L., and Shields, C.: Coupled climate simulation of
449 the evolution of global monsoons in the Holocene, *Journal of Climate*, 16(15), 2472-2490,
450 2003.

451 Mohtadi, M., Prange, M., and Steinke, S.: Palaeoclimatic insights into forcing and response of
452 monsoon rainfall, *Nature*, 533, 191-199, 2016.

453 Peng, S.Z., and Guo, Z.T.: Geochemical indicator of original eolian grain size and implications
454 on winter monsoon evolution, *Science in China Series D: Earth Sciences*, 44: 261-266, 2001.

455 Porter, S. C.: Chinese loess record of monsoon climate during the last glacial–interglacial cycle.
456 *Earth-Science Reviews*, 54(1-3): 115-128, 2001.

457 Rasmussen, S.O., Andersen, K.K., Svensson, A.M., Steffensen, J.P., Vinther, B.M., Clausen,
458 H.B., Siggaard-Andersen, M.L., Johnsen, S.J., Larsen, L.B., Dahl-Jensen, D., Bigler, M.,
459 Röhlisberger, R., Fischer, H., Goto-Azuma, K., Hansson, M.E., and Ruth, U.: A new
460 Greenland ice core chronology for the last glacial termination, *Journal of Geophysical*
461 *Research: Atmospheres*, 111(D6), 2006.

462 Reimer, P.J., Baillie, M.G.L., Bard, E., Bayliss, A., Beck, J.W., Bertrand, C.J.H., Blackwell, P.G.,
463 Buck, C.E., Burr, G.S., Cutler, K.B., Damon, P.E., Edwards, R.L., Fairbanks, R.G.,
464 Friedrich, M., Guilderson, T.P., Hogg, A.G., Hughen, K.A., Kromer, B., McCormac, G.,
465 Manning, S., Ramsey, C.B., Reimer, R.W., Remmele, S., Southon, J.R., Stuiver, M.,
466 Talamo, S., Taylor, F.W., van der Plicht, J., and Weyhenmeyer, C.E.: IntCal04 terrestrial
467 radiocarbon age calibration, 0-26 cal kyr BP, *Radiocarbon*, 46 (3), 1029-1058, 2004.

468 Reimer, P.J., Bard, E., Bayliss, A., Beck, J.W., Blackwell, P.G., Bronk Ramsey, C., Buck, C.E.,
469 Cheng, H., Edwards, R.L., and Friedrich, M.: IntCal13 and Marine13 radiocarbon age
470 calibration curves 0-50,000 years cal BP, *Radiocarbon*, 55, 1869-1887, 2013.

471 Richter, T. O., Van der Gaast, S., Koster, B., Vaars, A., Gieles, R., de Stigter, H. C., Haas, H.D.,
472 and van Weering, T. C.: The Avaatech XRF Core Scanner: technical description and
473 applications to NE Atlantic sediments, Geological Society, London, Special Publications,
474 267(1), 39-50, 2006.

475 Sagawa, T., Kuwae, M., Tsuruoka, K., Nakamura, Y., Ikehara, M., and Murayama, M.: Solar
476 forcing of centennial-scale East Asian winter monsoon variability in the mid-to late
477 Holocene. *Earth and Planetary Science Letters*, 395: 124-135, 2014.

478 Shala, S., Helmens, K., Jansson, K., Kylander, M., Risberg, J., and Lowemark, L.:
479 Palaeoenvironmental record of glacial lake evolution during the early Holocene at Sokli,
480 NE Finland, *Boreas*, 43: 362-376. doi: 10.1111/bor.12043, 2014.

481 Steinhilber, F., Beer, J., and Fröhlich, C.: Total solar irradiance during the Holocene[J].
482 *Geophysical Research Letters*, 36(19), 2009.

483 Stuiver, M., and Quay, P.D.: Changes in atmospheric carbon-14 attributed to a variable sun,
484 Science, 207 (4426), 11-19, 1980.

485 Sun, Y.B., Chen, J., Clemens, S.C., Liu, Q.S., Ji, J.F., and Tada, R.: East Asian monsoon
486 variability over the last seven glacial cycles recorded by a loess sequence from the
487 northwestern Chinese Loess Plateau, *Geochemistry, Geophysics, Geosystems*, 7 (12), 2006.

488 Sun, Y.B., Clemens, S.C., Morrill, C., Lin, X.P., Wang, X.L., and An, Z.S.: Influence of Atlantic
489 meridional overturning circulation on the East Asian winter monsoon, *Nature Geoscience*, 5
490 (1), 46-49, 2012.

491 Sun, Y.B., Liang, L.J., Bloemendal, J., Li, Y., Wu, F., Yao, Z.Q., and Liu, Y.G.: High -
492 resolution scanning XRF investigation of Chinese loess and its implications for millennial
493 - scale monsoon variability, *Journal of Quaternary Science*, 31(3), 191-202, 2016.

494 Tan, M.: Circulation effect: response of precipitation $\delta^{18}\text{O}$ to the ENSO cycle in monsoon
495 regions of China. *Climate Dynamics*, 42(3-4): 1067-1077, 2014.

496 Van Espen, P., Nullens, H., and Adams, F.: A computer analysis of X-ray fluorescence spectra,
497 *Nuclear Instruments and Methods*, 142(1-2), 243-250, 1977.

498 Wang, L., Li, J.J., Lu, H.Y., Gu, Z.Y., Rioual, P., Hao, Q.Z., Mackay, A.W., Jiang, W.Y., Cai,
499 B.G., Xu, B., Han, J.T., and Chu, G.Q.: The East Asian winter monsoon over the last 15,000
500 years: its links to high-latitudes and tropical climate systems and complex correlation to the
501 summer monsoon, *Quaternary Science Reviews*, 32, 131-142, 2012.

502 Wang, Y.J., Cheng, H., Edwards, R.L., He, Y., Kong, X., An, Z.S., Wu, J., Kelly, M.J., Dykoski,
503 C.A., and Li, X.: The Holocene Asian monsoon: links to solar changes and North Atlantic
504 climate, *Science*, 308, 854-857, 2005.

505 Weltje, G. J., and Tjallingii, R.: Calibration of XRF core scanners for quantitative geochemical
506 logging of sediment cores: theory and application, *Earth and Planetary Science Letters*,
507 274(3-4), 423-438, 2008.

508 Wen, X.Y., Liu, Z.Y., Wang, S.W., Cheng, J., and Zhu, J.: Correlation and anticorrelation of the
509 East Asian summer and winter monsoons during the last 21,000 years, *Nature*
510 *Communications*, 7, 11999, 2016.

511 Xiao, S.B., Li, A.C., Liu, J.P., Chen, M.H., Xie, Q., Jiang, F.Q., Li, T.G., Xiang, R., and Chen,
512 Z.: Coherence between solar activity and the East Asian winter monsoon variability in the
513 past 8000 years from Yangtze River-derived mud in the East China Sea. *Palaeogeography*,
514 *Palaeoclimatology, Palaeoecology*, 237(2-4): 293-304, 2006.

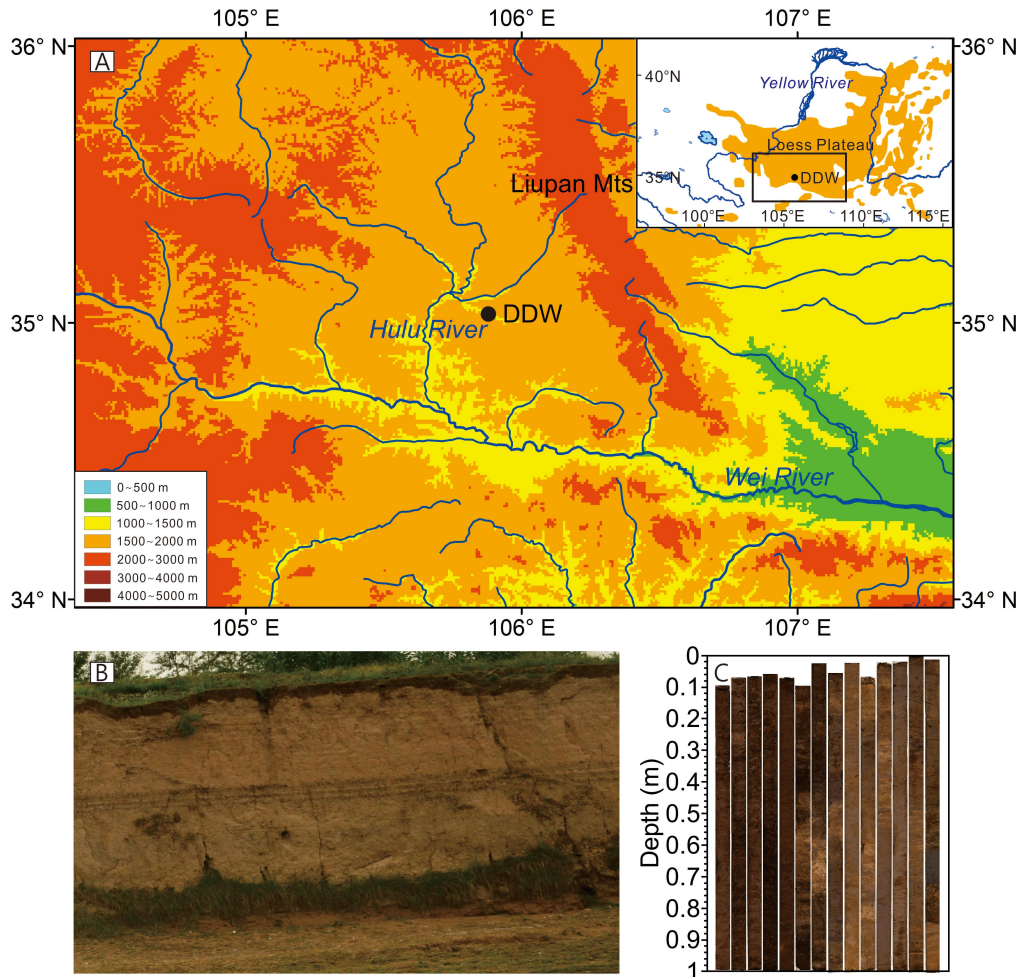
515 Yan, H., Soon, W., and Wang, Y.: A composite sea surface temperature record of the northern
516 South China Sea for the past 2500 years: a unique look into seasonality and seasonal
517 climate changes during warm and cold periods, *Earth-Science Reviews*, 141, 122-135, 2015.

518 Yancheva, G., Nowaczyk, N.R., Mingram, J., Dulski, P., Schettler, G., Negendank, J.F.W., Liu,
519 J., Sigman, D.M., Peterson, L.C., and Haug, G.H.: Influence of the intertropical
520 convergence zone on the East Asian monsoon, *Nature*, 445, 74-77, 2007.

521 Zhang, D. E., and Lu, L.: Anti-correlation of summer/winter monsoons?. *Nature*, 450(7168), E7,
522 2007.

523 Zhou, W.J., Zhao, X.L., Lu, X.F., Liu, L., Wu, Z.K., Cheng, P., Zhao, W.N., and Huang, C.H.:
524 The 3MV multi-element AMS in Xi'an, China: unique features and preliminary tests,
525 *Radiocarbon*, 48(2), 285-293, 2006.

526

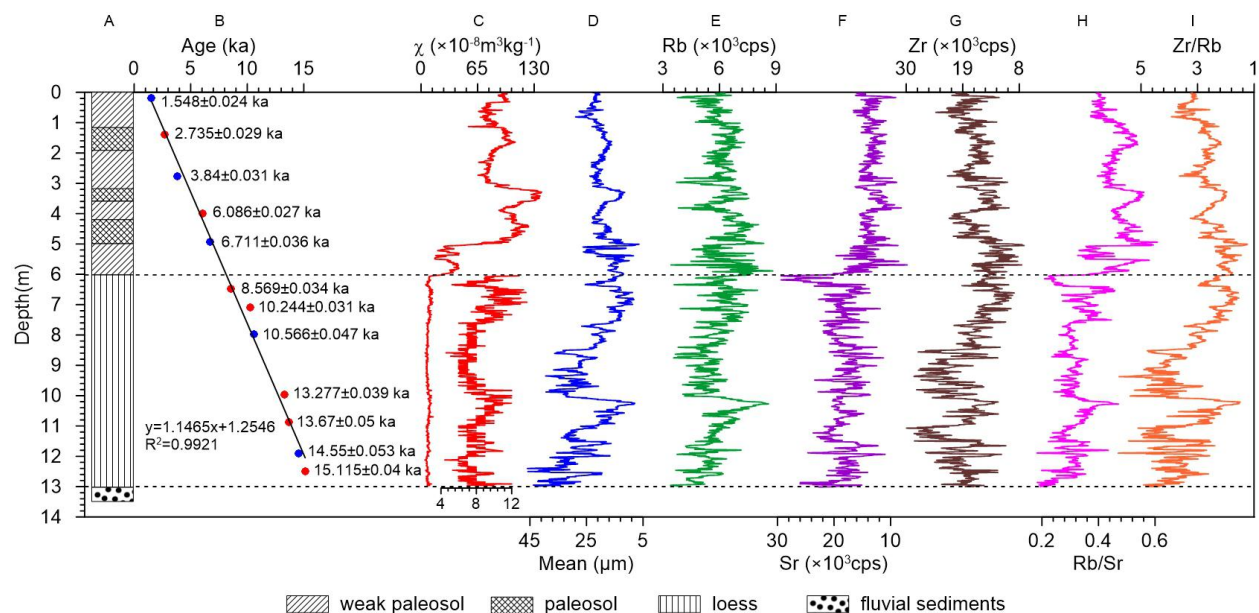


528

529 Fig 1. Map showing the CLP and location of the DDW (A), photographs of DDW terrace

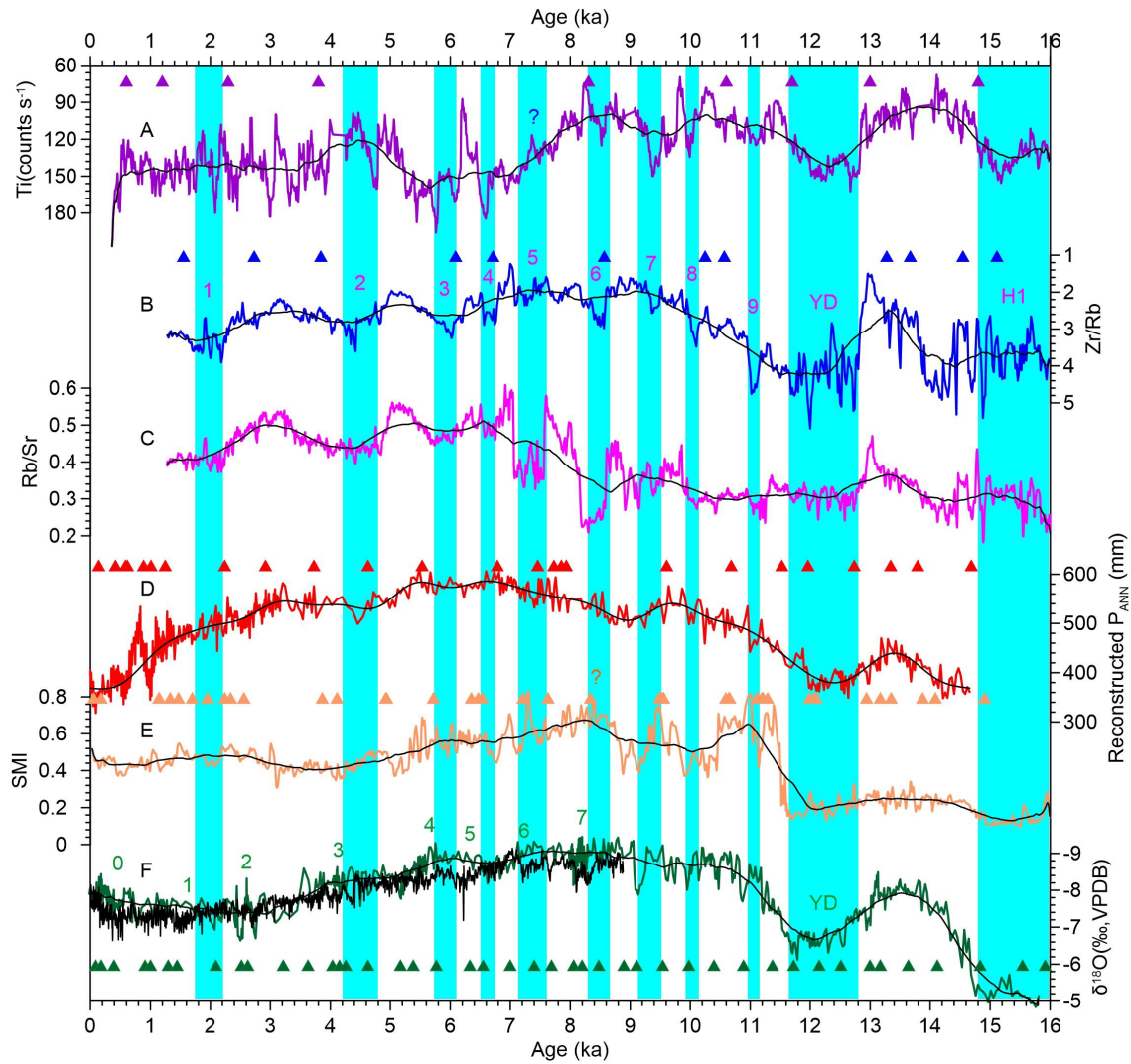
530 outcrop (B) and cores (C).

531



532
 533 Fig 2. Stratigraphy (A), age-depth model (B), magnetic susceptibility (C), grain-size results (D)
 534 and elemental results (E, F, G, H, I) measured by scanning XRF of the DDW core. Five red dots
 535 are ages in previous work (Liu et al., 2018). Blue dots are seven additional ages in this study.
 536 The elemental results were smoothed with a 3-point moving average.

537

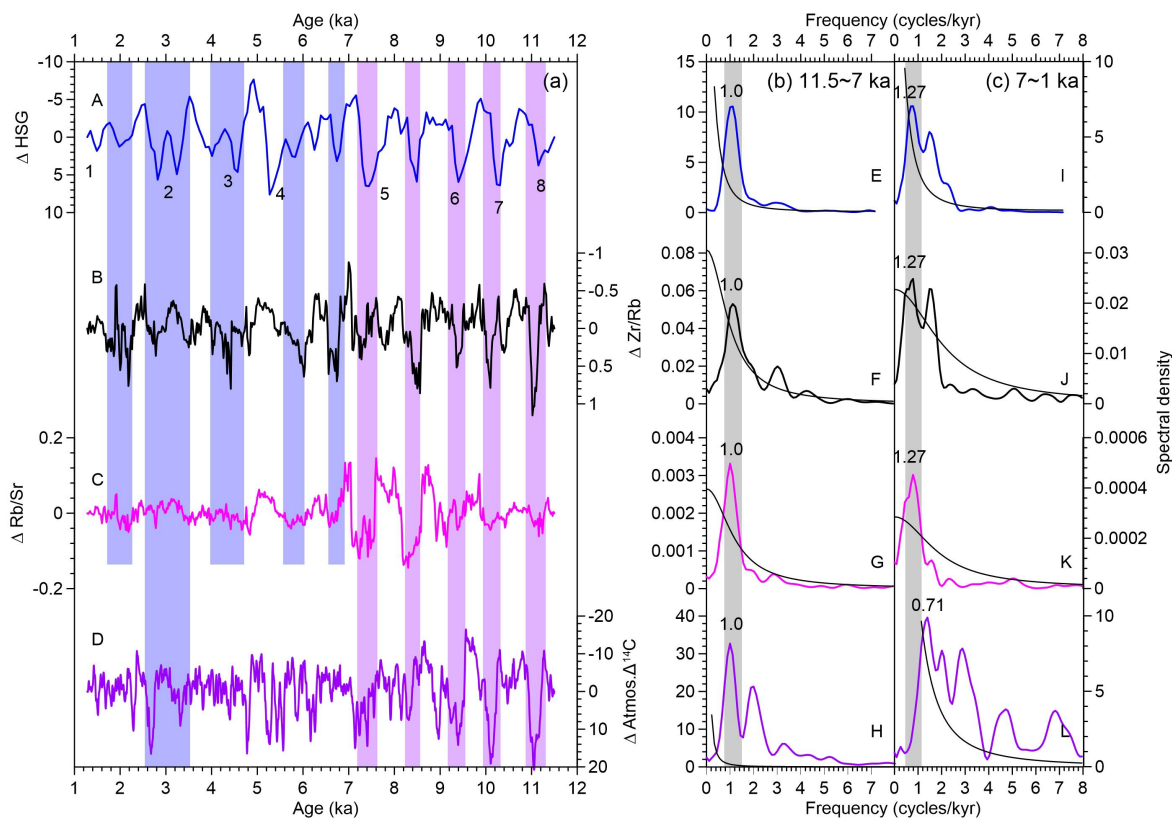


538

539 Fig 3. Comparisons of DDW records and other paleoclimatic records. (A) Ti content of Lake
 540 Huguang Maar (Yancheva et al., 2007); (B) Zr/Rb of DDW core; (C) Rb/Sr of DDW core; (D)
 541 Pollen-based annual precipitation (PANN) reconstructed from Gonghai Lake (Chen et al., 2015);
 542 (E) Lake Qinghai summer monsoon index (SMI) (An et al., 2012); (F) Speleothem $\delta^{18}\text{O}$ from
 543 Dongge Cave (Dykoski et al., 2005; Wang et al., 2005). AMS ^{14}C ages are marked on the records
 544 of Lake Huguang Maar (Purple triangle), DDW (Blue triangle), Gonghai Lake (Red triangle),
 545 and Lake Qinghai (Peach triangle), respectively. The ^{230}Th ages (Green triangle) are shown on

546 the speleothem records. The cyan bars indicate the timing of abrupt monsoon events in different
 547 records.

548



549
 550 Fig 4. Centennial components (a) of Zr/Rb (B) and Rb/Sr (C) with the North Atlantic HSG
 551 (Bond et al., 2001) (A) and atmosphere $\Delta^{14}\text{C}$ record (Reimer et al., 2013) (D). The purple and
 552 blue bars indicate abrupt monsoon events. The right panel shows the spectra of the proxy records
 553 during the early (b) and late Holocene (c). Spectral peaks that are above the 80% confidence
 554 levels (black lines) are marked. The grey vertical bands indicate the most significant cycle.

555